Fitting the two-compartment model in DCE-MRI by linear inversion

Dimitra Flouri[1,2], Daniel Lesnic[2] and Steven Sourbron[1]

Division of Biomedical Imaging [1] and Department of Applied Mathematics[2], University of Leeds, Leeds LS2 9JT, UK

Abstract

Purpose

Model fitting of DCE-MRI data with non-linear least squares (NLLS) methods is slow and may be biased by the choice of initial values. The aim of this study was to develop and evaluate a linear least-squares (LLS) method to fit the two-compartment exchange and -filtration models.

Methods

A second-order linear differential equation for the measured concentrations was derived where model parameters act as coefficients. Simulations of normal and pathological data were performed to determine calculation time, accuracy and precision under different noise levels and temporal resolutions. Performance of the LLS was evaluated by comparison against the NLLS.

Results

The LLS method is about 200 times faster, which reduces the calculation times for a 256×256 MR slice from 7min to 2sec. For ideal data with low noise and high temporal resolution the LLS and NLLS were equally accurate and precise. The LLS was more accurate and precise than the NLLS at low temporal resolution, but less accurate at high noise levels.

Conclusion

The data show that the LLS leads to a significant reduction in calculation times, and more reliable results at low noise levels. At high noise levels the LLS causes significant bias and should only be used when parameter accuracy is not important.

Key words

Dynamic Contrast-Enhanced Magnetic Resonance Imaging, tracer-kinetics, two-compartment model, linear least-squares method, non-linear least-squares method

INTRODUCTION

Dynamic contrast-enhanced magnetic resonance imaging MRI (DCE-MRI) involves the serial acquisition of T1-weighted MR images before, during, and after an intravenous administration of contrast agent. Tracer-kinetic analysis of the data produces physiological parameters such as tissue blood flow, capillary permeability, and the volume of the extravascular, extracellular space (1).

The most common class of tracer-kinetic models are the multi-compartment models, which are also widely used in other modalities such as positron-emission tomography (PET) and computed tomography (CT). Current standards in DCE-MRI are the two- or three parameter Patlak and Tofts models $(2, 3)$, which do not produce a measurement of tissue blood flow. In recent years, the increasing availability of DCE-MRI at high temporal resolution has promoted the use of four-parameter flow-weighted

models such as the two-compartment exchange model (2CXM) (4) and the renal two-compartment filtration model (2CFM) (5,6).

Non-linear least squares (NLLS) methods are the most commonly used algorithms to fit the model to the data (7). They require a choice of initial values which is updated iteratively using gradient-descent type methods, until the difference between predicted and measured data is minimal. The process is slow, and there is a risk of convergence to local minima. If this happens the result is biased by the initial values. A potential solution is to repeat the fit over a grid of initial values, but this requires massive computing capacity for pixel-based analysis (8).

An alternative is the use of linear least squares (LLS) methods, which produce parameter estimates by solving a linear system of equations. This is a fast computation that always identifies a global minimum without the need for initial values. A classic LLS method is the Patlak plot (3), but in 2004 Murase (9) introduced a LLS method for the extended Tofts model. Simulations demonstrated that this improves calculation times significantly without an associated cost in accuracy and precision. The method is rapidly becoming a standard in applications of DCE-MRI (10–13).

A LLS method for the more general 2CXM and 2CFM has not yet been proposed in the field of DCE-MRI, but in nuclear medicine it is well-known that such more general models can be linearised too (14–19). The purpose of this study is to develop a LLS method for the 2CXM and 2CFM, and evaluate calculation time, accuracy and precision using simulated data. A standard NLLS with a single set of initial values is used as a point of comparison.

METHODS

Theory

Definitions

The 2CXM and 2CFM are depicted graphically in Figure 1. The key difference is that the flux out of the extravascular space is either directed back into the plasma space (2CXM) or directly to the outside (2CFM). Since the physiological interpretation of the parameters is not relevant for the purposes of the paper, the conventional notations of the 2CFM parameters (6) are modified to emphasize the symmetries and eliminate redundant notations.
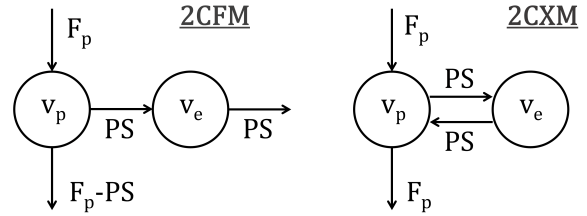

Figure 1: Diagrams of the 2CFM (left) and 2CXM (right).

The four independent model parameters are the plasma volume v_p, the extravascular volume v_e, the plasma flow F_p and the permeability-surface area product PS. The mean transit times of the blood (T_p), extravascular compartment (T_e) and combined system (T) have the same form in both models:

$$T_p = \frac{v_p}{F_p}, \qquad T_e = \frac{v_e}{PS}, \qquad T = \frac{v_p + v_e}{F_p} \qquad [1]$$

The measured tissue concentration $C(t)$ is a weighted average of the concentrations $c_p(t)$ and $c_e(t)$ in the individual spaces:

$$C = v_p c_p + v_e c_e \qquad [2]$$

The mass-balance for $c_e(t)$ is the same for both mod-

els (writing c'_e for the time-derivative of c_e):

$$v_e c'_e = PS(c_p - c_e) \qquad [3]$$

The difference between 2CXM and 2CFM lies in the mass-balance for $c_p(t)$. Given the arterial concentration $c_a(t)$, we have (4,6):

$$2\text{CFM} \quad : \quad v_p c'_p = F_p(c_a - c_p) \qquad [4]$$

$$2\text{CXM} \quad : \quad v_p c'_p = F_p(c_a - c_p) + PS(c_e - c_p) \quad [5]$$

We assume that $c_p(0) = c_e(0) = c_a(0) = 0$ which immediately leads to the initial conditions

$$C(0) = C'(0) = 0 \qquad [6]$$

Non-Linear Least Squares

The NLLS method is based on an explicit analytical solution of the models ($\otimes$ is convolution):

$$C(t) = F_p \left(\frac{T - T_-}{T_+ - T_-} e^{-t/T_+} + \frac{T_+ - T}{T_+ - T_-} e^{-t/T_-} \right) \otimes c_a(t) \qquad [7]$$

The difference between 2CXM and 2CFM lies in the relation between $T_\pm$ and the physiological parameters F_p, v_p, PS, v_e. The formulae are most straightforward in terms of the mean transit times (Eqs.[1]):

$$2\text{CFM} : T_+ = T_e, \qquad T_- = T_p \qquad [8]$$

$$2\text{CXM} : T_\pm = \frac{1}{2} \left(T + T_e \pm \sqrt{(T + T_e)^2 - 4T_p T_e} \right) \qquad [9]$$

The conventional NLLS method uses gradient-descent type techniques to minimise the mean-square difference between left- and right hand sides of Eq.[7].

Linear Least Squares

The LLS method is based on a reduction of the two first-order differential equations for the unmeasurable concentrations $c_p(t)$ and $c_e(t)$ (Eqs.[3,4,5]) to a single second-order differential equation for the measurable concentration $C(t)$ (Eq.[2]). The derivation follows a standard recipe that applies more generally to arbitrary N-compartment models (16).

For the 2CFM, differentiate Eq.[2] and use Eqs.[3,4] to eliminate c'_e and c'_p:

$$C' = F_p(c_a - c_p) + PS(c_p - c_e) \qquad [10]$$

Then apply the same procedure to Eq. [10]:

$$C'' = F_p c'_a - (F_p - PS)\frac{F_p}{v_p}(c_p - c_a) - PS\frac{PS}{v_e}(c_p - c_e) \qquad [11]$$

Equations [2,10,11] constitute a set of three differential equations with two unknown functions $c_p(t)$, $c_e(t)$. Eliminating them leads to a single second-order equation that only depends on the data C, c_a, and the unknown model parameters.

The same procedure can be applied to the 2CXM (Eqs.[3,5]). Expressing the result in terms of F_p, T, T_p, T_e leads to the same formula for both models:

$$C'' = -\alpha C - \beta C' + \gamma c_a + F_p c'_a \qquad [12]$$

The parameters (α, β, γ) are defined as:

$$2\text{CFM} : \alpha = \frac{1}{T_e T_p}, \quad \beta = \frac{T_e + T_p}{T_e T_p}, \quad \gamma = \frac{F_p T}{T_e T_p} \qquad [13]$$

$$2\text{CXM} : \alpha = \frac{1}{T_e T_p}, \quad \beta = \frac{T_e + T}{T_e T_p}, \quad \gamma = \frac{F_p T}{T_e T_p} \qquad [14]$$

To avoid the problems associated with the ill-posed numerical differentiation of noisy data, Eq.[12] can be integrated twice over time. Using the following notation for the integral:

$$\bar{f}(t) = \int_0^t f(\tau)\, d\tau \qquad [15]$$

this leads to:

$$C(t) = -\alpha \bar{\bar{C}}(t) - \beta \bar{C}(t) + \gamma \bar{\bar{c}}_a(t) + F_p \bar{c}_a(t) \quad [16]$$

3

If the data $C(t)$ and $c_a(t)$ are measured at N time points $t_0, t_1, \ldots, t_{N-1}$, then Eq.[16] leads to a system of N linear equations. They can be summarised as a matrix equation $\mathbf{C} = \mathbf{AX}$ where $\mathbf{C} = [C(t_0), \ldots, C(t_{N-1})]$ is an array holding the measured concentrations, and $\mathbf{X} = [\alpha, \beta, \gamma, F_p]$ contains the unknowns. The $4 \times N$-element matrix $\mathbf{A}$ is given explicitly by:

$$\mathbf{A} = \begin{pmatrix} -\bar{\bar{C}}(t_0) & -\bar{C}(t_0) & \bar{\bar{c}}_a(t_0) & \bar{c}_a(t_0) \\ -\bar{\bar{C}}(t_1) & -\bar{C}(t_1) & \bar{\bar{c}}_a(t_1) & \bar{c}_a(t_1) \\ \vdots & \vdots & \vdots & \vdots \\ -\bar{\bar{C}}(t_{N-1}) & -\bar{C}(t_{N-1}) & \bar{\bar{c}}_a(t_{N-1}) & \bar{c}_a(t_{N-1}) \end{pmatrix} \quad [17]$$

The matrix elements can be calculated via Eq.[15] by numerical integration of the data $C(t_n)$ and $c_a(t_n)$. The matrix equation can be solved using standard methods for linear least squares problems. Since the typical number of time points in DCE-MRI is in the 100's, and there are only 4 unknowns, this presents a strongly overdetermined system.

It remains to derive the physiological parameters T, T_e, T_p from given α, β, γ, F_p by inverting Eqs. [13,14]. For the 2CXM this is most straightforward:

$$T = \frac{\gamma}{\alpha F_p}, \quad T_e = \frac{\beta}{\alpha} - T, \quad T_p = \frac{1}{\alpha T_e} \quad [18]$$

In the 2CFM, the formula for T is the same, but T_e and T_p are the solutions of a quadratic equation:

$$T_p = \frac{\beta - \sqrt{\beta^2 - 4\alpha}}{2\alpha}, \quad T_e = \frac{\beta + \sqrt{\beta^2 - 4\alpha}}{2\alpha} \quad [19]$$

A second solution could be derived by reversing the roles of T_p and T_e, but in reality it is safe to assume that contrast agent passes faster through the microvasculature than through the extravascular space ($T_p < T_e$). Since α and β are measured there is no a priori guarantee that these solutions are real. In case they are not ($\beta^2 < 4\alpha$) the best solution in the least squares sense is:

$$T_p = T_e = \frac{\beta}{2\alpha} \quad [20]$$

The parameters v_p, v_e and PS can be derived from F_p, T, T_p, T_e by inverting Eqs. [1]:

$$v_p = F_p T_p, \qquad v_e = F_p(T - T_p), \qquad PS = \frac{v_e}{T_e} \quad [21]$$

Weighted Linear Least Squares (WLLS)

Eq. [16] can be generalised by multiplying both sides with an arbitrary weighting function $W(t)$:

$$WC = -\alpha\, W\bar{\bar{C}} - \beta\, W\bar{C} + \gamma\, W\bar{\bar{c}}_a + F_p\, W\bar{c}_a \quad [22]$$

With $W(t) = 1$ this reduces to the LLS, but a large number of possible weighting functions $W(t)$ could be used. To investigate the effect and potential of weighting we will consider in this study the strategy $W(t) = c_a(t)$. As the arterial input function is strongly weighted by the first pass data, one would expect this to improve the accuracy in the parameters F_p and T_p which are mainly determined by the high-frequency components occuring in this time window.

Simulation setup

Simulations were used to evaluate the sensitivity of the LLS to two important types of data error, random noise and temporal undersampling. As the analysis is very similar for 2CXM and 2CFM, simulations were only performed for the 2CFM and renal tissues to reduce the scope of the study. Simulations were written in IDL 6.4 (Exelis VIS, Boulder, CO) conducted on a desktop PC with a 3.4 GHz Intel Core processor and 32GB memory. All simulation code can be found online (https://github.com/plaresmedima/Linear-2CM).

To ensure a representative range of physiological parameters, five whole-kidney tissues were defined: one representing normal kidneys with parameter values measured in healthy volunteers (6), and four pathological kidneys taken from a recent patient study (20). Cases were selected by identifying the kidneys corresponding to the 10th and 90th percentiles in T_e and v_p. The parameters are summarised in Table 1.

	T_p (sec)	T_e (sec)	v_p	v_e
Normal	6.5	125	0.24	0.62
Patient 1	9.5	102	0.17	0.24
Patient 2	13.9	153	0.31	0.24
Patient 3	7.27	117	0.19	0.26
Patient 4	10.3	214	0.29	0.18

Table 1: Parameter values of the simulated data sets.

To generate an exact ground-truth $C(t)$, one of the five tissue types was selected at random with equal probability, and $C(t)$ was calculated with the analytical solution (Eq.[7]). A literature-based arterial input function $c_a(t)$ was used (21), prepadded with zeroes to create a 20s baseline. $C(t)$ and $c_a(t)$ were created at a pseudo-continuous temporal resolution of 10msec for times ranging from $t = 0s$ to a total of $T_{acq} = 300s$. All convolutions in this study are calculated using a formula that is optimised for convolutions with an exponential factor (see Appendix).

Measurements with a given uniform sampling interval TR (sec) and Contrast-to-Noise Ratio (CNR) were simulated. CNR is defined in this study as the ratio of peak arterial concentration to the standard deviation (SD) of the noise, ie. CNR = $\max(c_a)$/SD. The CNR range was between CNR=50 (worst-case of single-pixel curves) and CNR=500 (low-noise limit in ideal ROI-based curves). TR was chosen between TR=2.0s (high temporal resolution protocols for F_p-measurement) and TR=10.0s (low temporal resolution protocol for glomerular filtration rate (GFR) or PS assessment). The first time-point t_0 of the measurement was determined by selecting a random number from a uniform distribution on the interval [0,TR]. Then time-points $t_n = t_0 + n$TR were added with $n = 1, \ldots, N - 1$ and $N = \lfloor T_{acq}/\text{TR} \rfloor$. Downsampled $C(t_n)$ and $c_a(t_n)$ were created by interpolating linearly between the values of the pseudo-continuous curves, and Gaussian noise was added.

The LLS matrix (Eq. [17]) was calculated by numerical integration of the measured $C(t_n)$ and $c_a(t_n)$ using the trapezoidal rule. The least-squares system was solved by inverting the 4×4 normal equations, i.e. $\mathbf{X} = (\mathbf{A}^T\mathbf{A})^{-1}\mathbf{A}^T\mathbf{C}$. The NLLS was implemented by fitting the analytical solution (Eq. [7]) using the Levenberg-Marquardt algorithm with the function MPFIT (22). Convolutions were calculated with the iterative formula in the Appendix. Partial derivatives with respect to the model parameters were calculated numerically and default values were used for the termination tolerance (10^{-3}) and maximum number of iterations (200). No constraints were placed on any of the parameters, and fixed initial values were used. They were taken at approximately half the exact values in normal tissue to avoid a bias with respect to a particular tissue type ($T_p = 3s$, $T_e = 60s$, $v_p = 0.1$, $v_e = 0.3$).

For each reconstruction P_i of a parameter $P = F_p, PS, T_p, T_e$, the error $E_i(P)$ was determined as a percentage of the exact value:

$$E_i(P) = 100 * \frac{P_i - P}{P} \qquad [23]$$

The goodness-of-fit was quantified in a similar way as the relative distance between the fitted concentra-

tions $C_i^{\text{fit}}(t_n)$ and measured concentrations $C_i^{\text{msr}}(t_n)$:

$$E_i(C) = 100 * \frac{\|C_i^{\text{fit}} - C_i^{\text{msr}}\|_2}{\|C_i^{\text{msr}}\|_2} \qquad [24]$$

Simulations for given TR and CNR were repeated 10,000 times to determine the distribution of results. The median relative error E_{50} was recorded as a measure of the systematic error, and the 90% confidence interval CI $= E_{95} - E_5$ as a measure of the random error.

The performance of the LLS or WLLS was quantified via two figures of merit (FoM), one for the accuracy and one for the precision:

$$\text{FoM (Accuracy)} = |E_{50}(\text{NLLS})| - |E_{50}(\text{LLS})| \quad [25]$$

$$\text{FoM (Precision)} = \text{CI(NLLS)} - \text{CI(LLS)} \qquad [26]$$

A positive (negative) FoM means that the LLS improves (reduces) the accuracy or precision. Numerically, a FoM of 1% implies that LLS reduces the systematic or random error by 1% of the exact parameter value.

FoM's were determined explicitly for 3 different protocols representing boundary regimes: protocol 1 at high temporal resolution and high noise level (TR=2.0s and CNR=50), protocol 2 at the opposite regime of low temporal resolution and low noise level (TR=10s and CNR=500), and protocol 3 under ideal conditions of high temporal resolution and low noise (TR=2.0s and CNR=500).

RESULTS

Figure 2 provides an illustration of the data and model fits at the highest noise level considered in this study. The plots show that the fit to the data is significantly poorer with LLS than with NLLS, which provides an almost exact reconstruction of the underlying concentrations despite high levels of noise.

The LLS method is faster than the NLLS method by a factor of 210, i.e. two orders of magnitude. In absolute terms, for an MR image of 256×256 pixels the computation time on a laptop PC is 2 sec and 7 min for the LSS and NLLS methods, respectively.

Table 2 provides the FoM's under the ideal circumstances of protocol 3 (low noise and high temporal resolution). The results show that LLS leads to a small improvement in accuracy (0.5% on average) but a loss in precision (-2.9% on average). There is no benefit in adding a weighting with WLLS.

Figure 3 shows that the differences in accuracy and precision are small under the ideal conditions of protocol 3. The distinction between LLS and NLLS is most pronounced in the parameter F_p, where NLLS and LLS produce relative errors in the range $1.0\% \pm 3.5\%$ and $0.02\% \pm 4.0\%$, respectively (median $\pm$ half of 90% CI).

Table 3 provides the FoM's under conditions of low noise and low temporal resolution (protocol 2). Under these conditions the LLS shows a clear improvement in accuracy ($+5.7\%$ on average) and precision in all parameters, and there is again no benefit in weighting with WLLS. The gain in precision is $+2300\%$ on average, but this is largely determined by an outlier (T_e). Excluding this, the gain is precision is still $+70\%$ on average.

Figure 4 visualises the transition in the low-noise regime from protocol 3 (high temporal resolution) to protocol 2 (low temporal resolution) in more detail. The figure shows that the improved accuracy and precision of the LLS persists across the whole range of temporal resolutions, becoming gradually more pronounced towards protocol 2 at the low temporal resolution (right side of the plot).

Table 4 provides the FoM's under the opposite conditions of high noise and high temporal resolution

(protocol 1). In this regime the LLS is associated with a significant loss in accuracy in all parameters (-40% on average). Adding weighting improves the error in all parameters, but the accuracy is still lower than with NLLS (-10% on average). The effect on precision depends on the parameter. LLS causes a major loss in precision for T_p (-160%), but improves the precision of the other parameters. Adding a weight reduces the loss in T_p but the effect remains significant and also leads to a reduction in precision of F_p.

Figure 5 visualises the transition in the high temporal resolution regime from protocol 3 (low noise) to protocol 1 (high noise). The figure shows that the errors increase in a systematic manner with CNR, showing the strong noise-sensitivity of LLS. For a measurement targeting the vascular parameters F_p and T_p, the NLLS is more reliable at all noise levels. The NLLS is also preferred for the permeability parameters PS and T_e, except in the high-noise limit of protocol 1 where the WLLS is the optimal.

	LLS		WLLS	
	Accuracy	Precision	Accuracy	Precision
F_p	10	90	-4.2	9.7
T_p	7.2	39	-11	-140
PS	2.1	76	1.2	-36
T_e	3.4	9100	-5.0	8700

Table 3: Figures of Merit (FoM) for LLS and WLLS for protocol 2 at low noise level (CNR=500) and low temporal resolution (TR=10.0s).

	LLS		WLLS	
	Accuracy	Precision	Accuracy	Precision
F_p	-24	2.6	-2.6	-13
T_p	-65	-162	-9.4	-47
PS	-47	83	-24	40
T_e	-23	8900	-4	9200

Table 4: Figures of Merit (FoM) for LLS and WLLS for protocol 1 at high noise level (CNR=50) and high temporal resolution (TR=2.0s).

	LLS		WLLS	
	Accuracy	Precision	Accuracy	Precision
F_p	0.93	-3.1	0.34	-3.9
T_p	0.99	-3.5	0.22	-3.3
PS	0.13	-2.4	-0.06	-1.9
T_e	0.081	-2.7	0.10	-3.2

Table 2: Figures of Merit (FoM) for LLS and WLLS for protocol 3 under ideal conditions of low noise level (CNR=500) and high temporal resolution (TR=2.0s).

DISCUSSION

As expected, the LLS leads to a massive reduction in computation time with a factor 210. The current study showed a reduction from 7 min to 2 sec for a 256×256 matrix, but the total saving depends on computing hardware, implementation details, and the number of time points in the data. It also depends on the implementation of the NLLS. In this study a fixed initial value was used rather than a grid of initial values, and in that sense the estimate of NLLS calculation time represents a best case scenario. The improvement in calculation time is not of practical significance for an ROI-based analysis, where other steps in the analysis form the main bottlenecks (eg. data transfer, segmentation). However for a pixel-based analysis the improvement may have significant implications for clinical practice. The effect may also be important for other methods that use pixel-based tracer-kinetic modeling as an intermediate step, such as model-based segmentation or registration techniques, or data undersampling strategies
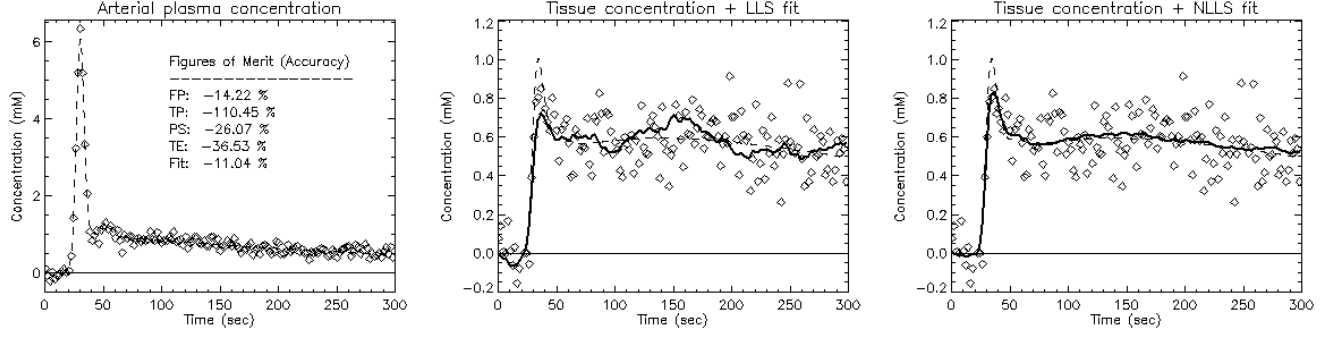
Figure 2: Example of the exact concentrations (dashed line) and a simulated measurement for protocol 1 at TR=2.0s and CNR=50 (diamonds). The figure shows results in the arterial plasma (left), and the tissue with an overlay of the LLS fit (full line, middle) and NLLS fit (full line, right). The insert (left) gives the Figures of Merit for each of the parameters in this particular case.
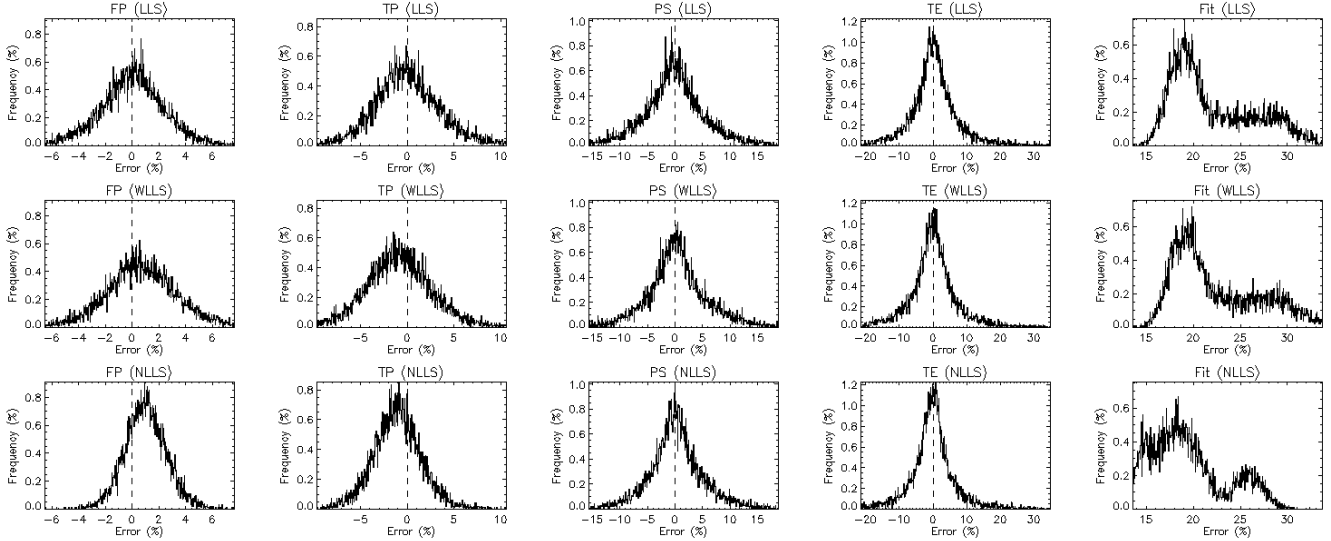

Figure 3: The error distribution for protocol 3 under ideal conditions of low noise level (CNR=500) and high temporal resolution (TR=2.0s). Results are shown for each method (LLS - top row, WLLS - middle row, NLLS - lower row) and for each parameter (F_p - column 1, T_p - column 2, PS - column 3, T_e - column 4, goodness-of-fit - column 5).
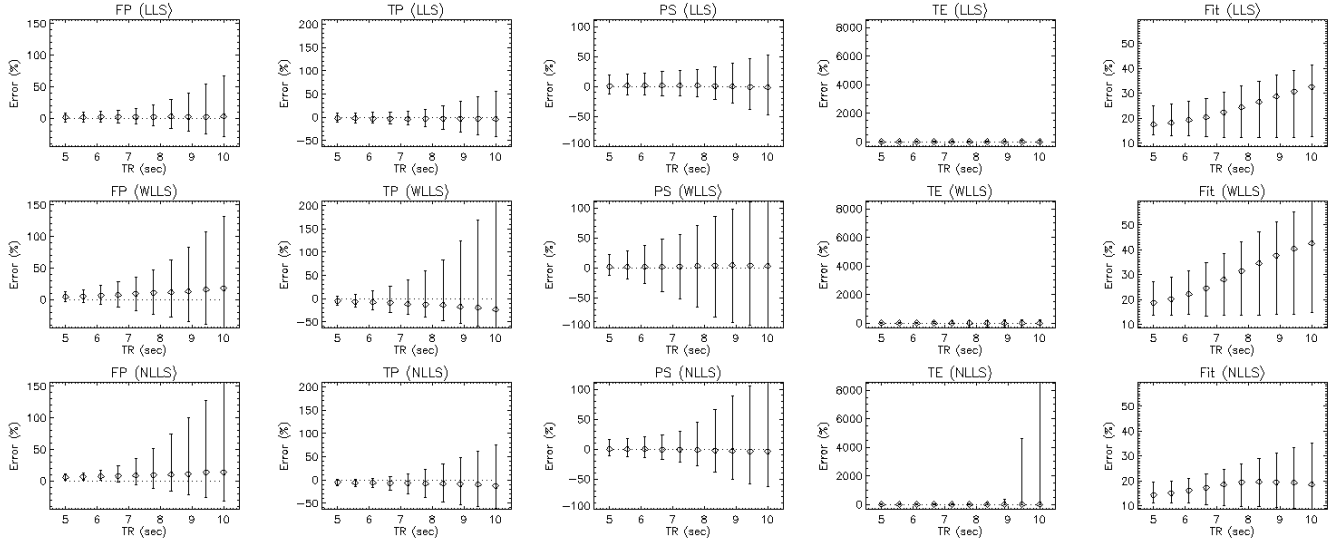
Figure 4: Error distribution at fixed CNR=500 (low noise level) but variable TR. The circles indicate the median error and the error bars represent the 90% confidence interval. Results are shown for each method (LLS - top row, WLLS - middle row, NLLS - lower row) and for each parameter (F_p - column 1, T_p - column 2, PS - column 3, T_e - column 4, goodness-of-fit - column 5).
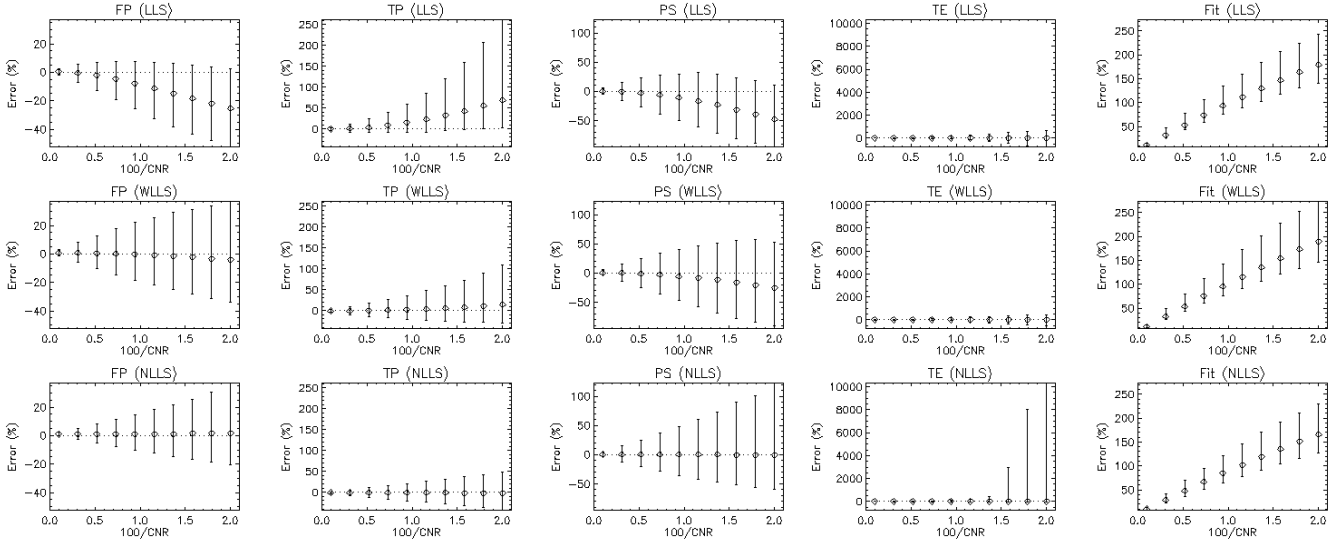

Figure 5: Error distribution at fixed TR=2.0s (high temporal resolution) but variable CNR with a minimum of CNR=50. The circles indicate the median error and the error bars represent the 90% confidence interval. Results are shown for each method (LLS - top row, WLLS - middle row, NLLS - lower row) and for each parameter (F_p - column 1, T_p - column 2, PS - column 3, T_e - column 4, goodness-of-fit - column 5).

using the temporal structure as a constraint.

The effect of LLS on accuracy and precision is more ambiguous. Key observations are summarised in Figure 6. As a general rule, the LLS is preferred at low-noise conditions and the NLLS at high temporal resolution. In the ideal conditions where these two regimes meet (protocol 3), their performance is comparable and both can be used interchangeably. The NLLS is slightly more reliable as the gain in precision offsets the loss in accuracy, but the differences are small and not likely to be significant for clinical applications. In that sense, the LLS may be preferred in view of its computational benefit. There is no benefit of adding a weighting with $W(t) = c_a(t)$ except for the leakage parameters under conditions of very high noise and high temporal resolution (protocol 1). This regime is less relevant as all measurements are unreliable under these conditions. For the same reasons the regime of low temporal resolution and high noise level is not of practical interest (upper right corner of Fig. 6).

The systematic error of the LLS at higher noise levels is unexpected from an MRI perspective as previous experiences with the linearised extended Tofts model have shown an improved accuracy at higher noise levels (9, 23). In part, this discrepancy may be due to implementation differences in the NLLS between the current and previous studies (9). However, it is likely that the effect is mostly due to the added complexity of a 2nd-degree linear model. A key difference with the extended Tofts model is that the linearised equation of the 2CXM or 2CFM contains a second-order derivative. This leads to the double integrals in Eq.[16] which effectively add a strong weight on the later time points where little temporal structure is available. As a result the solution becomes less well determined than in the NLLS,
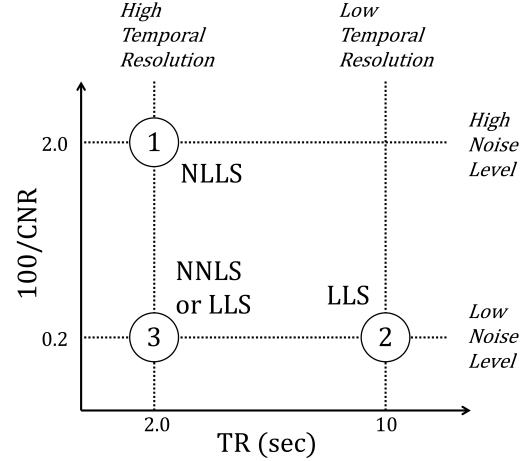

Figure 6: Summary of the observations regarding accuracy and precision. The figure maps different experimental conditions in the TR - CNR plane showing the location of the three protocols for which the Figures-of-Merit have been simulated (circles) and the different limiting regimes of high/low noise level and high/low temporal resolution (dotted lines). Optimal choices of methods (NNLS, LLS) are indicated next to the respective protocols.

10

where the first-pass data carry a strong weight due to the high signal values in this regime. This is also consistent with the observation that a weighting factor $W(t) = c_a(t)$ reduces the systematic errors significantly: at high temporal resolution the function $c_a(t)$ is dominated by the first pass where most of the temporal structure can be found. The chosen weighting does not remove the error completely, but alternative weighting strategies have not been explored and could lead to further improvement. An alternative solution that may be worth considering is the use of the differential form combined with temporal filtering to improve the noise sensitivity (23). However, it is not clear whether this remains beneficial in second order.

In the nuclear medicine literature it is well-known that LLS methods for 4-parameter 2-compartment models cause a bias in the parameters (14–16, 19, 24, 25). There is no a priori guarantee that these observations translate to DCE-MRI (or DCE-CT). Noise levels, temporal resolutions and acquisition times generally lie in entirely different regimes. A more fundamental difference lies in the typical data structure of first-pass DCE-MRI or -CT, where all high-frequency information is stored in a narrow and early time interval. This explains why the weighting effect of the double integration is more significant in DCE-MRI. Nevertheless, our study confirms that LLS at high noise levels causes a bias in all DCE-MRI parameters.

This raises the question of whether the solutions proposed for PET could help to reduce the bias. Feng et al. (15,16) proposed a generalized linear least squares (GLLS) method, which has found some use in pixel-based parameter estimation for PET (26). However a more recent comparative study indicated that it still exhibits large bias and poor precision at higher noise levels (19). Zeng et al. (18) proposed a more general weighted integration method to address the problem. Instead of integrating the linear equation (Eq.[11]) twice over time, it is multiplied with wavelets $g(t, T)$ on a support $t \in [0, T]$, and integrated once over that interval. Despite appearances, this method is not fundamentally different from double integration, and it is identical when the wavelets are chosen as $g(t, T) = T - t$. This follows from the identity:

$$\int_0^T dt \, (T - t) f(t) = \bar{\bar{f}}(T) \qquad [27]$$

Hence, one would not expect an improved performance. Zeng et al. (18) did not observe a bias, but the scope of their simulations was limited and restricted to data with low temporal resolution and relatively low noise levels. This corresponds roughly to the low-noise regime where we have also observed that the LLS is more robust (Figure 6). The wavelet-based method does have the advantage that different families of wavelets can be used, but there is no evidence that this would eliminate the observed bias.

CONCLUSION

The LLS method for solving the 2CXM or 2CFM reduces the computation times by two orders of magnitude, and is at least as accurate and precise as the NLLS at low noise levels. At higher noise levels the LLS is exceedingly inaccurate and should only be used when parameter accuracy is not so important.

Appendix

The NLLS implementation in this study uses an efficient and accurate iterative algorithm for the evaluation of a convolutions with an exponential factor:

$$f(t) = a(t) \otimes \frac{e^{-t/T}}{T} \equiv \frac{1}{T} \int_0^t d\tau \, a(\tau) \, e^{-(t-\tau)/T} \quad [A1]$$

The algorithm applies to situations where the function $a(t)$ is measured and thus only available at discrete times $t_0 = 0, t_1, t_2, \ldots, t_{n-1}$ (not necessarily uniformly spaced).

With $T = 0$ the result is $f(t) = a(t)$. With $T \neq 0$ the integral is evaluated by interpolating linearly between the values $a_i = a(t_i)$, leading to an iterative formula with starting value $f(t_0) = 0$:

$$f(t_{i+1}) = e^{-x_i} f(t_i) + a_i E_0(x_i) + a_i' T E_1(x_i) \quad [A2]$$

where

$$E_0(x) = \int_0^x e^{-(x-u)} du = 1 - e^{-x} \quad [A3]$$

$$E_1(x) = \int_0^x u e^{-(x-u)} du = x - E_0(x) \quad [A4]$$

and

$$x_i \equiv \frac{t_{i+1} - t_i}{T}, \qquad a_i' \equiv \frac{a_{i+1} - a_i}{t_{i+1} - t_i} \quad [A5]$$

Compared to standard numerical convolution, Eq. [A2] is more accurate because the exponential factor is not approximated. It is also more efficient computationally due to its iterative nature.

To prove the results, consider first the case $T = 0$:

$$\lim_{T \to 0} \frac{e^{-t/T}}{T} * a(t) = \delta(t) * a(t) = a(t) \quad [A6]$$

For any other T, note that the initial value is $f(t_0) = 0$ since $t_0 = 0$. Now given $f(t_i)$, the value $f(t_{i+1})$ can be determined by splitting up the integral and

substituting $u = (\tau - t_i)/T$:

$$\frac{1}{T} \int_0^{t_{i+1}} d\tau \, a(\tau) \, e^{-(t_{i+1}-\tau)/T}$$

$$= \frac{1}{T} \int_0^{t_i} d\tau \, a(\tau) \, e^{-(t_{i+1}-\tau)/T}$$

$$+ \frac{1}{T} \int_{t_i}^{t_{i+1}} d\tau \, a(\tau) \, e^{-(t_{i+1}-\tau)/T}$$

$$= \frac{1}{T} \int_0^{t_i} d\tau \, a(\tau) \, e^{-x_i - (t_i - \tau)/T}$$

$$+ \int_0^{x_i} du \, a(t_i + Tu) \, e^{-(x_i - u)}$$

$$\approx e^{-x_i} f(t_i) + \int_0^{x_i} du \, (a_i + a_i' Tu) \, e^{-(x_i - u)}$$

Eq. [A2] then follows directly from the definitions [A3,A4]. The linear interpolation between data points is made in the second term of the last line, and is the only approximation made.

References

[1] Sourbron SP, Buckley DL. Tracer kinetic modelling in MRI: estimating perfusion and capillary permeability. Phys Med Biol 2012;57: R1−R33.

[2] Tofts PS, Brix G, Buckley DL, et al. Estimating kinetic parameters from dynamic contrast-enhanced T1-weighted MRI of a diffusable tracer: Standardized quantities and symbols. J Magn Reson Imaging 1999;10:223−232.

[3] Patlak CS, Blasberg RG. Graphical evaluation of blood-to-brain transfer constants from multiple-time uptake data. Generalizations. J Cereb Blood Flow Metab 1985;5:584−590.

[4] Brix G, Kiessling F, Lucht R, Darai S, Wasser K, Delorme S, Griebel J. Microcirculation and microvasculature in breast tumors: pharmacokinetic analysis of dynamic MR image series. Magn Reson Med 2004;52:420−429.

[5] Annet L, Hermoye L, Peeters F, Jamar F, Dehoux JP, Van Beers BE. Glomerular filtration rate: assessment with dynamic contrast-enhanced MRI and a cortical-compartment model in the rabbit kidney. J Magn Reson Imaging 2004;20:843−849.

[6] Sourbron SP, Michaely HJ, Reiser MF, Schoenberg SO. MRI-measurement of perfusion and glomerular filtration in the human kidney with a separable compartment model. Invest Radiol 2008;43:40−48.

[7] Ahearn TS, Staff RT, Redpath TW, Semple SI. The use of the Levenberg-Marquardt curve-fitting algorithm in pharmacokinetic modelling of DCE-MRI data. Phys Med Biol 2005;50:N85−N92.

[8] Leporq B, Camarasu-Pop S, Davila-Serrano E, Pilleul F, Beuf O. Enabling 3D-Liver Perfusion Mapping from MR-DCE Imaging Using Distributed Computing. J Med Eng 2013;471682.

[9] Murase K. Efficient method for calculating kinetic parameters using T1-weighted dynamic contrast-enhanced magnetic resonance imaging. Magn Reson Med 2004;51: 858−862.

[10] Cárdenas-Rodríguez J, Howison CM, Pagel MD. A linear algorithm of the reference region model for DCE-MRI is robust and relaxes requirements for temporal resolution. J Magn Reson Imaging. 2013;31:497−507.

[11] Li J, Yu Y, Zhang Y, Bao S, Wu C, Wang X, Li J, Zhang X, Hu J. A clinically feasible method to estimate pharmacokinetic parameters in breast cancer. Aapm. 2009;36:3786−3794.

[12] Adluru G, DiBella EV, Schabel MC. Model-based registration for dynamic cardiac perfusion MRI. J Magn Reson Imaging 2006;24:1062−1070.

[13] Faranesh AZ, Kraitchman DL, McVeigh ER. Measurement of kinetic parameters in skeletal muscle by magnetic resonance imaging with an intravascular agent. J Magn Reson Medicine 2006;55:1114−1123.

[14] Wen L, Eberl S, Fulham MJ, Feng D, Beng J. Constructing reliable parametric images using enhanced GLLS for dynamic SPECT. IEEE Trans Biomed Eng 2010;56:1117−1126.

[15] Feng D, Wang ZZ, Huang SC, Wang ZZ, Ho D. An unbiased parametric imaging algorithm for nonuniformly sampled biomedical system parameter estimation. IEEE Trans Med Imaging 1996;15:512−518.

[16] Feng D, Ho D, Chen K, Wu LC, Wang JK, Liu RS, Yeh SH. An evaluation of the algorithms for determining local cerebral metabolic rates of glucose using positron emission tomography dynamic data. IEEE Trans Med Imaging 1995;14:697−710.

[17] Zeng GL, Kadrmas DJ, Gullberg GT. Fourier domain closed-form formulas for estimation of kinetic parameters in multi-compartment models. IEEE Nuclear Science Symposium and Medical Imaging Conference Record 2011;3209−3216.

[18] Zeng GL, Hernandez A, Kadrmas DJ, Gullberg GT. Kinetic parameter estimation using a closed-form expression via integration by parts. Phys Med Biol 2012;57:5809−5821.

[19] Dai X, Chen Z, Tian J. Performance evaluation of kinetic parameter estimation methods in dynamic FDG-PET studies. Nucl Med Commun 2011;32:4−16.

[20] Lim SW, Chrysochou C, Buckley DL, Kalra PA, Sourbron SP. Prediction and assessment of responses to renal artery revascularization with dynamic contrast-enhanced magnetic resonance imaging: a pilot study. Am J Physiol Renal Physiol 2013;305:672−678.

[21] Parker GJ, Roberts C, Macdonald A, et al. Experimentally-derived functional form for a population-averaged high-temporal-resolution arterial input function for dynamic contrast-enhanced MRI. Magn Reson Med 2006;56:993−1000.

[22] Markwardt, CB. Non-Linear Least Squares Fitting in IDL with MPFIT. In: Proceedings Astronomical Data Analysis Software and Systems XVIII 2009;411:251−254.

[23] Wang C, Yin F-F, Chan, Z. An efficient calculation method for pharmacokinetic parameters in brain permeability study using dynamic contrast-enhanced MRI. Magn Reson Med. 2015. Online ahead of print.

[24] Cai W, Feng D, Fulton R, Siu W-C. Generalized linear least squares algorithms for modeling glucose metabolism in the human brain with corrections for vascular effects. Comput Methods and Programs Biomed 2002;68:1−14.

[25] Ichise M, Toyama H, Innis RB, Carson RE. Strategies to improve neuroreceptor parameter estimation by linear regression analysis. J Cereb Blood Flow Metab 2002;22:1271−1281.

[26] Chen K, Lawson M, Reiman E, et al. Generalized linear least squares method for fast generation of myocardial blood flow parametric images with N-13 ammonia PET. IEEE Trans Med Imaging 1998;17:236−243.